nuclear fusion

PAPER • OPEN ACCESS

Overview of recent results from the ST40 compact high-field spherical tokamak

To cite this article: S.A.M. McNamara *et al* 2024 *Nucl. Fusion* **64** 112020

OPEN ACCESS
IOP Publishing | International Atomic Energy Agency

Nuclear Fusion

Nucl. Fusion **64** (2024) 112020 (14pp)

https://doi.org/10.1088/1741-4326/ad6ba7

Overview of recent results from the ST40 compact high-field spherical tokamak

S.A.M. McNamara[1,*], A. Alieva[1], M.S. Anastopoulos Tzanis[1], O. Asunta[1], J. Bland[1], H. Bohlin[1], P.F. Buxton[1], C. Colgan[1], A. Dnestrovskii[1], E. du Toit[1], M. Fontana[1], M. Gemmell[1], M.P. Gryaznevich[1], J. Hakosalo[1], M.R. Hardman[1], D. Harryman[1], D. Hoffman[1], M. Iliasova[1], S. Janhunen[1], F. Janky[1], J.B. Lister[1], H.F. Lowe[1], E. Maartensson[1], C. Marsden[1], S.Y. Medvedev[1], S.R. Mirfayzi[1], M. Moscheni[1], G. Naylor[1], V. Nemytov[1], J. Njau[1], T. O'Gorman[1], D. Osin[1], T. Pyragius[1], A. Rengle[1], M. Romanelli[1], C. Romero[1], M. Sertoli[1], V. Shevchenko[1], J. Sinha[1], A. Sladkomedova[1], S. Sridhar[1], J. Stirling[1], Y. Takase[1], P.R. Thomas[1], J. Varje[1], E. Vekshina[1], B. Vincent[1], H.V. Willett[1], J. Wood[1], E. Wooldridge[1], D. Zakhar[1], X. Zhang[1], D. Battaglia[2,a,b], N. Bertelli[2], P.J. Bonofiglo[2], L.F. Delgado-Aparicio[2], V.N. Duarte[2], N.N. Gorelenkov[2], M. de Haas[2], S.M. Kaye[2], R. Maingi[2], D. Mueller[2], M. Ono[2], M. Podesta[2,b], Y. Ren[2], S. Trieu[2], E. Delabie[3], T.K. Gray[3], B. Lomanowski[3], E.A. Unterberg[3], O. Marchuk[4] and the ST40 Team[1]

[1] Tokamak Energy Ltd Milton Park, Oxfordshire OX14 4SD, United Kingdom of Great Britain and Northern Ireland
[2] Princeton Plasma Physics Laboratory, Princeton, NJ 08543, United States of America
[3] Oak Ridge National Laboratory, Oak Ridge, TN 37831, United States of America
[4] Forschungszentrum Jülich GmbH, Institut für Energie- und Klimaforschung-Plasmaphysik, Partner of the Trilateral Euregio Cluster (TEC), 52425 Jülich, Germany

E-mail: steven.mcnamara@tokamakenergy.com

Received 28 February 2024, revised 11 July 2024
Accepted for publication 6 August 2024
Published 29 August 2024

CrossMark

Abstract

ST40 is a compact, high-field ($B_{T0} \leqslant 2.1$ T) spherical tokamak (ST) with a mission to expand the physics and technology basis for the ST route to commercial fusion. The ST40 research programme covers confinement and stability; solenoid-free start-up; high-performance operating scenarios; and plasma exhaust. In 2022, ST40 obtained central deuterium ion temperatures of 9.6 ± 0.4 keV, demonstrating for the first time that pilot plant relevant ion temperatures can be reached in a compact, high-field ST. Analysis of these high-ion temperature plasmas is presented, including a summary of confinement, transport and microstability characteristics, and energetic particle instabilities. Recent scenario development activities have focused on establishing diverted H-mode plasmas across a range of toroidal fields and plasma currents, along with scenarios with high non-inductive current fractions. In future operations, beginning in 2025, a 1 MW dual frequency (104/137 GHz) electron cyclotron (EC) system

[a] Current address: Commonwealth Fusion Systems, Devens, MA 01434, United States of America.
[b] Current address: Ecole Polytechnique Fédérale de Lausanne, Swiss Plasma Center, CH-1015 Lausanne, Switzerland.
[*] Author to whom any correspondence should be addressed.

will be installed to enable the study of EC and electron Bernstein wave plasma start-up and current drive. Predictive modelling of the potential performance of these systems is presented.

Keywords: spherical tokamak, high-field, ST40, overview

(Some figures may appear in colour only in the online journal)

1. Introduction

ST40 is a compact high-field spherical tokamak (ST) with copper magnets, built and operated by Tokamak Energy Ltd, a private company based in Oxfordshire, UK, which is developing commercial fusion power plants based on the combination of the ST and high-field magnets made from REBCO high temperature superconductor (HTS). The goal of ST40 is to expand the physics basis for the ST, by exploring confinement and transport; solenoid free plasma start-up; exhaust properties; and high-performance operating scenarios at toroidal magnetic fields over twice that previously achieved in other STs.

Spherical tokamaks offer an attractive route to commercial fusion due to their enhanced stability properties [1] and more favourable transport and confinement properties when compared to conventional aspect ratio devices [2]. Combined with high-field magnets made from high temperature superconductor this opens a route to more compact and potentially reduced cost fusion power plants.

The paper summarises progress on ST40 between 2021–2023. During this period there were two main operational phases, referred to as Programme 2.2 and Programme 2.3. Programme 2.2, which ran from March 2021–February 2022, focused on achieving plasma ion temperatures in excess of 100 million degrees Kelvin (8.6 keV), which was a key business milestone. Programme 2.3 began in June 2023 and is divided into multiple Campaigns, the first of which, Campaign 1, ran until September 2023 and was focused on exploring and expanding the operating space and range of achievable scenarios, with a particular focus on developing H-mode diverted scenarios and scenarios with high non-inductive current fractions.

This paper is arranged as follows. Section 2 introduces the ST40 device and its diagnostics, as well as providing an overview of the integrated data analysis framework used throughout the paper. The next three sections summarise results from Programme 2.2. Section 3 describes the high ion temperature scenarios, where a central deuterium temperature of 9.6 ± 0.4 keV was achieved. Section 4 provides an overview of confinement and stability studies, summarising transport properties of the high ion temperature scenarios and the first study of the dependence of energy confinement time on ion mass. Section 5 provides a summary of energetic particle instabilities and an overview of a possible interplay between energetic particle modes and H-L back transitions. In section 6, predictive modelling of electron cyclotron and electron Bernstein wave heating and current drive is presented, in anticipation of the installation of the 1MW dual frequency (104/137 GHz) gyrotron system in 2025. Finally, section 7 describes recent efforts in developing diverted H-mode scenarios and scenarios with a high non-inductive current fraction.

Research on ST40 is partly supported by a first-of-a-kind private-public fusion partnership funded by the U.S. Department of Energy Office of Science. This partnership enables staff from Oak Ridge National Laboratory (ORNL) and Princeton Plasma Physics Laboratory (PPPL) to participate actively in research activities on ST40, including contributing to plasma operations and diagnostic implementation.

2. The ST40 high-field spherical tokamak

2.1. ST40 overview

ST40 is a compact high-field spherical tokamak, with main parameters shown in table 1. The maximum toroidal field is over twice that of any other ST. Plasma heating is provided by two neutral beams injected tangentially in the co-current direction that deliver approximately 0.9 MW at 55 kV and 0.7 MW at 24 kV when operated in deuterium. The maximum injected pulse duration for the 55 kV and 24 kV beams is 200 ms and 90 ms respectively. In the 2023/2024 shutdown work is underway to increase the duration of the 24 kV beam. The 55 kV beam heats both the ions and electrons and was chosen to provide central power deposition with minimal shine through [3]. The 24 kV beam has a wider deposition profile, primarily heats the ions and provides significant core fuelling. A 1 MW dual-frequency (104/137 GHz) gyrotron has been ordered and is due to be installed 2024 with operations beginning in 2025.

Plasma start-up is achieved using Merging Compression (MC), where two high-voltage in-vessel poloidal field coils inductively initiate the plasma. MC start-up has been demonstrated on several tokamaks [4–8] and allows direct access to high plasma currents without using the central solenoid. The process involves three stages [8]. Firstly, the two high-voltage in-vessel PF coils (called the 'MC coils' in ST40) are ramped to full current and gas is injected into the vessel. The MC coil current is then ramped down, generating a large loop voltage that causes the plasma to breakdown and form two helical rings around the MC coils. In the second stage, the large loop voltage induces a significant plasma current within the two rings, until at some point the attractive force between the two plasma rings overcomes that of the rings and the MC coils causing the rings to 'pinch-off' from the MC coils and move towards each other. Finally, magnetic reconnection occurs and the two plasma rings merge and are compressed radially towards the centre column to form a tokamak plasma. During this final stage, poloidal magnetic energy is

Table 1. The main parameters of the ST40 high-field spherical tokamak.

Major radius	$R_{\mathrm{Geo}} = 0.4 - 0.5\,\mathrm{m}$
Minor radius	$a = 0.25 - 0.33\,\mathrm{m}$
Aspect ratio	$A = 1.6 - 1.9$
Elongation	$\kappa < 2.0$
Triangularity	$\delta < 0.6$
Torodial magnetic field	$B_{\mathrm{T0}} = 0.9 - 2.1\,\mathrm{T}$
Plasma current	$I_{\mathrm{p}} = 0.25 - 0.8\,\mathrm{MA}$
Installed neutral beam power	$P_{\mathrm{NB}} = 1.8\,\mathrm{MW}$
Planned radio-frequency power	$P_{\mathrm{RF}} = 1.0\,\mathrm{MW}$

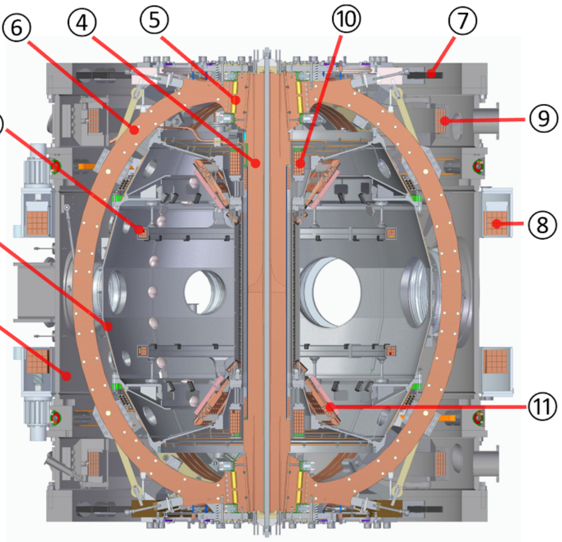

Figure 1. A cross-section of the ST40 high-field spherical tokamak showing (1) in-vessel merging compression coils, (2) inner vacuum chamber, (3) outer vacuum chamber, (4) TF centre column consisting of 24 twisted wedges and overwound solenoid, (5) TF flexible joints, (6) TF return limbs, (7) pre-tensioned carbon bands, (8) BVL coils, (9) BVU coils, (10) DIV coils and (11) the divertor assemblies.

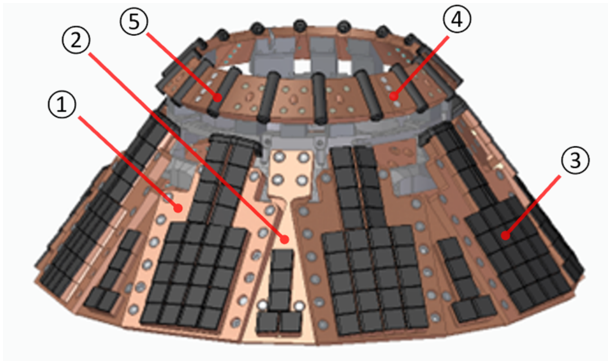

Figure 2. The ST40 divertor assembly comprising of (1) 8 nickel plated copper carriers, (2) 8 bridging plates, (3) molybdenum plated copper chromium zirconium tiles that form the plasma facing surface, (4) toroidally conducting aluminium alloy passive stabilisation ring and (5) 16 graphite limiter strips.

converted into kinetic energy via reconnection, predominantly heating the plasma ions to keV temperatures. A central solenoid, providing approximately 200 mVs of inductive flux, is used to increase and sustain the plasma current flat-top, which can last up to 250 ms. An impurity powder dropper constructed by Tokamak Energy and based on concepts developed at PPPL [9], has recently been installed. This system is capable of injecting multiple powder species, such as lithium, boron, carbon or various compounds, with different particulate sizes with a resolution of <0.1 mg. This system will be used in future operations for vessel conditioning and plasma impurity seeding.

An engineering model of ST40 is shown in figure 1. ST40 has an inner vacuum chamber (IVC) providing the ultra-high vacuum required for plasma operations and an outer vacuum chamber (OVC) that acts as a mechanical support structure. ST40 was originally designed to operate with the toroidal field (TF) and some of the poloidal field (PF) coils cryogenically cooled using liquid nitrogen. To enable this, the OVC can be sealed with two domes that cover the top and bottom of the cyrostat. However, due to technical and programmatic reasons, ST40 has not yet operated with liquid nitrogen cooling and there are no plans in the immediate future to do so. As a result, the OVC domes have not been installed and the maximum toroidal field is limited to 2.1 T. The toroidal field coilset has 24 turns and comprises of a centre column containing 24 twisted wedges, each with a toroidal angular displacement of 15° along their length to provide continuity of the TF circuit, and 24 return limbs grouped in 8 packs of 3. The return limbs are electrically connected to the centre column wedges using copper-copper pressed joints and mechanically isolated using copper foil flexibles. The out of plane electromagnetic loads, resulting from interactions with the TF and PF coils, are reacted to the OVC by a system of pre-tensioned carbon bands. These bands provide high stiffness and strength with minimal thermal conduction. ST40 has 3 pairs of poloidal field coils, which provide the shaping and control fields. These are refereed to as the BVL and BVU coils, for vertical field (B_{v}) lower and upper respectively, and DIV coils, which are used to create the diverted configuration. The BVL coils provide the bulk vertical field and radial position control, the BVU coils provide shaping and fast vertical control, and the DIV coils are used to form the diverted configuration.

Upper and lower divertor assemblies, one of which is shown in figure 2, comprise of 8 nickel plated copper carriers connected by 8 bridging plates, which provide structural support and form a toroidally conducting passive stabilisation ring to enable operations with increased plasma elongations. The plasma facing surface is made of molybdenum plated copper chromium zirconium tiles mounted on each carrier and angled to prevent exposure of leading edges. Each divertor assembly also has a toroidally conducting aluminium alloy passive stabilisation ring with 16 graphite limiter strips to provide additional vertical stabilisation. The ST40 divertor assemblies were installed *in situ* using one of the larger midplane ports to gain access to the vessel.

This placed limits on the size and weight of each component in the assembly.

2.2. ST40 diagnostics and integrated analysis

ST40 is equipped with numerous diagnostics. A full set of magnetic field and flux sensors are used for real-time magnetic control and post-pulse magnetic reconstruction. The plasma position and shape are determined in real-time using an in-house reconstruction code, PFIT, which estimates the plasma current centroid position and last closed flux surface, enabling both plasma current centroid position and gap control. Between shots, equilibrium reconstruction is produced using EFIT [10], with a magnetics-only reconstruction available after every pulse, and work on adding kinetic and other constraints on-going. The line integrated electron density is measured using a radial sub millimetre (SMM) interferometer system running at 0.94 mm and 0.91 mm. A visible survey spectrometer and line-filtered diodes (D_α, D_β, C-II, C-III, O-II, O-III) are used for low-Z impurity and Bremsstrahlung monitoring. A suite of diagnostics comprising of foil based bolometers, multi-element AXUV diodes (cameras) and single-element AXUV diodes are used to provide measurements of the radiated power. Two foil based bolometers [11] and two AXUV cameras provide tangential horizontal and radial vertical views of the plasma. The AXUV cameras each have a fan of 16 lines of sight and the horizontal and vertical bolometers have 8 and 12 lines of sight respectively. These cameras are used to provide tomographic measurements of the radiated power profile. The AXUV cameras have two channels, one with no window and the second with a 25 μm Be filter. The unfiltered channel provides fast bolometer-like measurements of the radiated power. Four filtered AXUV diodes, sharing a single line-of-sight through the plasma, provide a time-resolved measurement of the line-integrated soft x-ray (SXR) emission. Different filters are used for each diode (10 μm Be, 250 μm Be, 50 μm Al, and 250 μm Al), and the diagnostic thereby works as a coarse four-channel spectrometer based on the x-ray transmission of the metal foils. These systems will be used to provide information on the radiated power profiles, plasma composition, be able to resolve core MHD activity (with the AXUV camera operating at 100 kHz), and determine the sawtooth inversion radius.

Fusion neutrons are detected using diamond detectors and scintillation spectrometers, both of which are capable of resolving the 2.45 MeV and 14.1 MeV neutrons originating from the plasma. The detectors can distinguish between neutrons and gamma rays using methodology based on total charge deposition and pulse shape analysis, respectively [12]. Additionally, hard x-rays are recorded using NaI scintillation detectors, which are calibrated to generate a gamma spectrum. High-resolution fast visible (10 kHz) and D_α (1 kHz) cameras view the main chamber and part of the upper/lower divertors. An IR camera views the central column and parts of the divertor regions. A high spectral resolution x-ray crystal spectrometer (XRCS) diagnostic [13], measures electron and ion temperatures in the core region across a single LOS viewing radially across the midplane, and it requires a small prefill puff of argon in every shot. The XRCS ion temperature is obtained from the He-like Argon resonance line w and the electron temperature from the k/w and n = 3/w line ratios. A visible charge-exchange recombination spectroscopy (CXRS) system [13] using a conventional grating spectrometer from Princeton Instruments, viewing the C-VI 529 nm and Ne-X 525 nm spectral lines, measures ion temperature and toroidal rotation profiles along 6 lines of sight intersecting the 24 keV heating neutral beam. A second spectrometer (TriWaSp—Triple wavelength spectrometer) with a higher input numerical aperture allows a greater signal collection and improved signal-to-noise ratio on three different spectral regions using 3 grisms [14]. The grisms are chosen to view simultaneously on the same lines of sight: (i) deuterium (main ion) at 656 nm for T_i, V_{rot}, fast-ion D_α (FiDa) and beam emission spectroscopy (BES) studies; (ii) B-V line at 494 nm; and (iii) C-VI and Ne-X at 529 and 525 nm respectively. The TriWaSp is currently configured to view the 55 keV HNBI beam in a near tangential configuration. A 15-channel neutral particle analyser (NPA) measuring neutral hydrogenic particle fluxes at energies between 1–41 keV provides information on the fast ion distribution function.

Since the completion of Programme 2.2 a range of new diagnostic systems have been installed. These included a dedicated fast (0.8 kHz) high-resolution (640 $\times$ 512 pixels with 0.2 mm spatial resolution) divertor-IR camera, installed in collaboration with Oak Ridge National Laboratory, which views the upper outer divertor strike surface and is used to measure the scrape-off-layer width and edge plasma conditions; an array of 6 embedded single Langmuir probes installed in the upper and lower outer divertor targets, which operate in sweep mode measuring ion saturation current, electron temperature and density; an 8 channel foil bolometer viewing the upper divertor [11]; and a Thomson scattering (TS) system for measuring electron temperature and density profiles [15]. The TS system uses a 100 Hz, 1 J, Nd:YAG laser with a 8 ns pulse width, and measures 30 spatial points along a tangential line of sight along the midplane, passing close to the center column, with a varying spatial resolution across the plasma, ranging from $\sim$40 mm at the high-field side, to $\sim$20 mm at the plasma core, and with the highest resolution of $\sim$10 mm at the low-field-side pedestal region. An example image from the divertor IR camera and the corresponding heat flux profile fitted to using the Eich formalism for the scrape-off layer profile [16] is shown in figure 3.

To make the most of the available diagnostics in each plasma operation phase, forward models of various diagnostic systems are constantly being developed and exploited [17]. These are used to aid diagnostic design, provide consistency-checks of the instruments being commissioned, develop diagnostic analysis methods, as well as constrain higher-level parameters for discharge interpretation and modelling. In combination with other codes and databases such as Open-ADAS [18], FIDASIM [19], ASCOT [20] and NUBEAM [21], these forward models have been used to: design neutron diagnostics, bolometer and AXUV camera systems; test methodologies

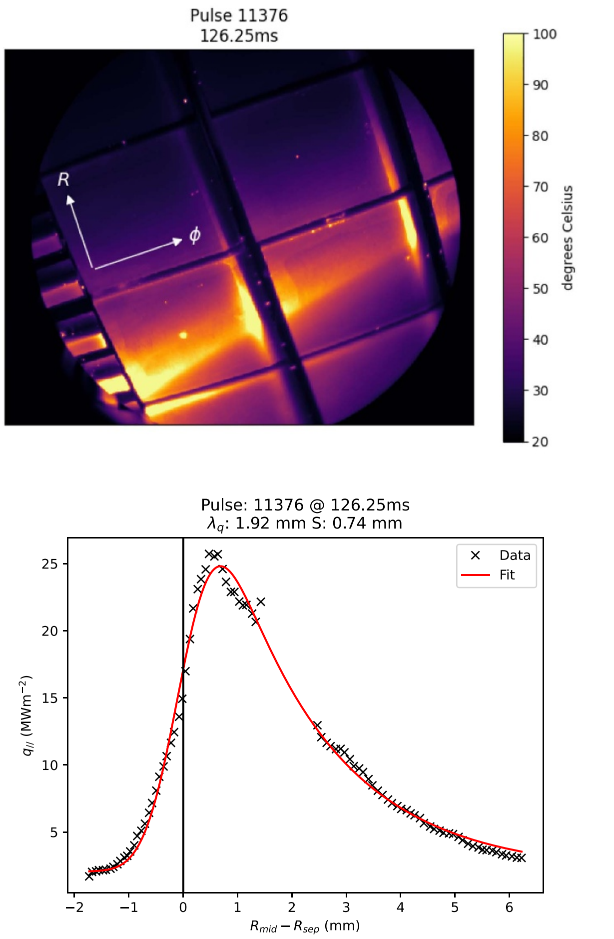

Figure 3. (Top) An example divertor IR camera image for pulse #11376. Each of the tiles are square with 3.5 cm side length. Some of the Langmuir probes are visible to the left of the image. (Bottom) Parallel heat flux, $q_{\|}$ as a function of distance from the separatrix ($R_{\mathrm{mid}} - R_{\mathrm{sep}}$) mapped from the divertor strike surface to the outer midplane (black crosses) and corresponding profile fitted using the Eich formalism for the scrape-off layer (red curve).

and uncertainties related to inverting/inferring radiation profiles with the limited set of LOS; assess potential of non-locality of the CXRS measurements close to the plasma edge due to spectral shearing/smearing; constrain the fueling source rate using the D-alpha camera; and aid the design, interpretation and calibration of the new TS diagnostic. The models have also been arranged in integrated analysis workflows using stepwise optimization algorithms and Bayesian methodologies. During the 2022 campaign, in the absence of profile diagnostics, the main application of these workflows was to constrain the kinetic profile shapes using a combination of XRCS, CXRS, SMM and EFIT measurements [22]. In the 2023 campaign, since the installation of the new Thomson scattering diagnostic, these workflows are being expanded and re-scoped to constrain the ion temperature profile, infer the effective charge profile using visible Bremsstrahlung, estimate 2D poloidal maps of the radiated power combining data from the AUXV cameras and bolometry, and other applications.

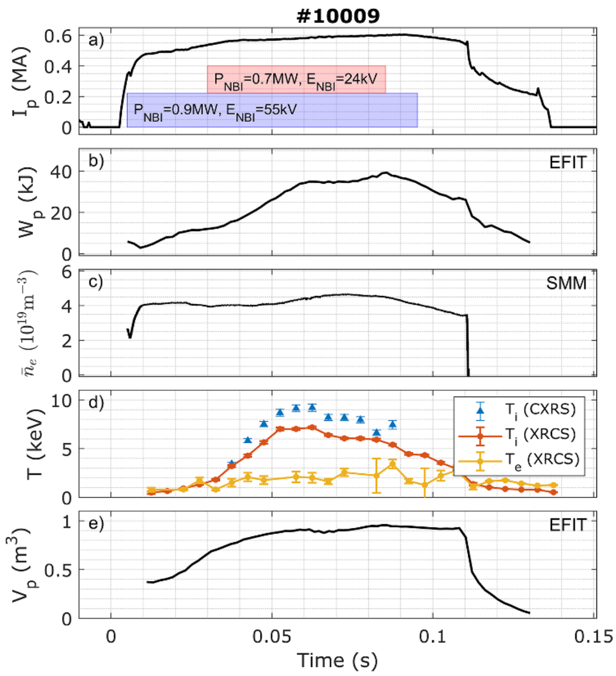

Figure 4. Overview of discharge #10009, showing (*a*) plasma current and neutral beam injection parameters, (*b*) stored energy, (*c*) line averaged electron density, (*d*) ion and electron temperatures measured using x-ray crystal spectroscopy viewing He-like Argon (XRCS) and CXRS, and (*e*) plasma volume. Reproduced from [22].

3. High ion temperature scenarios

In 2022, ST40 obtained a central deuterium ion temperature of 9.6 ± 0.4 keV, demonstrating for the first time that ion temperatures relevant for commercial fusion can be obtained in a compact, high-field ST [22]. Such high ion temperatures have previously only been reached in significantly larger devices and never in a ST. These high temperatures were achieved in hot-ion L-mode discharges, where $T_{\mathrm{i}} \gg T_{\mathrm{e}}$, in deuterium plasmas with deuterium neutral beam injection. Hot-ion modes generally share common features of centralised ion heating, low ion-electron collisional coupling to minimise power transfer from the hotter ions to cooler electrons, peaked density profiles, and suppression of turbulence leading to improved ion confinement.

By injecting 1.6 MW of neutral beam power into a plasma with an on-axis toroidal magnetic field of $B_{\mathrm{T0}} = 1.9$ T, plasma current $I_{\mathrm{p}} = 0.6$ MA and plasma of volume 0.9 m^3, carbon ion temperatures of 9.2 keV were measured using a charge exchange recombination spectroscopy (CXRS) system, where the most central line of sight measures approximately 1 cm from the magnetic axis [13]. Using the integrated analysis procedure described above, the on-axis carbon impurity temperature was estimated to be 9.8 keV, with a corresponding main ion temperature of 9.6 keV determined using TRANSP [23]. Parameters from one such high ion temperature discharge, #10009, are shown in figure 4

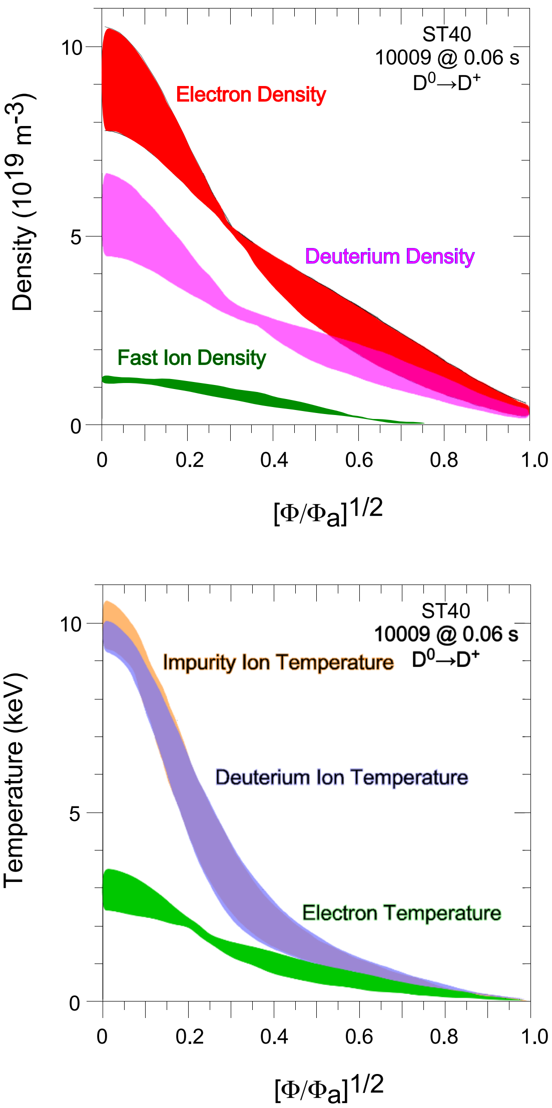

Figure 5. Profiles of (top) electron density, deuterium ion and fast ion densities, (bottom) impurity and deuterium ion, and electron temperatures determined using the integrated analysis approach for pulse #10009 at time of maximum ion temperature (60 ms). Reproduced from [24].

and the corresponding temperature and density profiles at the time of peak ion temperature, 60 ms, as determined using the integrated analysis procedure and TRANSP, are shown in figure 5. The effective ion charge, Z_{eff} is estimated to be 2 with the main impurity species assumed to be carbon, helium and argon. The total injected neutral beam power, P_{NB}, was 1.6 MW with 5%–8% shine through, the Ohmic heating power, P_{OH}, was 0.5 MW and the fast ions account for approximately 30% of the stored energy. Taking these values and the thermal stored energy, W_{th}, the energy confinement time, defined as $\tau_{\mathrm{E}} = W_{\mathrm{th}}/(P_{\mathrm{NB}} + P_{\mathrm{OH}} - dW_{\mathrm{th}}/dt)$, is calculated to be 15 ms and the corresponding fusion triple product is $n_{\mathrm{i0}} T_{\mathrm{i0}} \tau_{\mathrm{E}} \approx 6 \pm 2 \times 10^{18}$ m^{-3}keVs.

4. Confinement and stability

4.1. Transport and microstability properties of high temperature plasmas

The integrated analysis procedure described above was used to infer the T_{e}, T_{i}, and n_{e} profile ranges that were input into TRANSP to determine the plasma transport characteristics of the high performance, hot-ion mode plasmas [24]. Plasma density and temperature profiles for a high T_{i} are shown in figure 5. The fast ion (beam) density, as calculated in the NUBEAM Monte-Carlo code, was about 20% of the thermal deuterium density. The impurity ion temperature was input to TRANSP, which computed the deuterium ion temperature from power balance considerations. As can be seen, the TRANSP calculations based on these profile ranges indicated that hydrogenic ion temperatures were only 0.5–1.0 keV lower than those measured in the carbon impurity, reaching the 10 keV level.

The TRANSP power balance calculations for this discharge are shown in figure 6 for the electrons (left panel) and ions (middle panel). In each frame, power sources are plotted as positive numbers, and the losses are plotted as negative numbers. A comparison of the electron and ion channels show that electrons were the primary loss channel through thermal conduction. For the ions, the beam thermalisation (beam ions slowing down to $<5/2T_{\mathrm{i}}$) was comparable to the direct collisional heating of the thermal ions by the beams, and the energy loss through ion-electron coupling (energy flow from ions to electrons due to $T_{\mathrm{i}} > T_{\mathrm{e}}$) was comparable to the thermal conduction loss. The thermal diffusivity profiles (figure 6(right panel)) reflect the power balance results, with $\chi_{\mathrm{e}} > \chi_{\mathrm{i}}$ across the entire profile. While the ion thermal diffusivity was very low in the plasma center ($< \chi_{\mathrm{neoclassical}}$), reflecting the fact that it was, to a large extent, reduced central ion transport that led to high T_{i}, the ion thermal transport in these hot-ion mode plasmas was much greater than neoclassical in the mid- and outer regions of the plasma.

Linear gyrokinetic stability analysis of ST40 hot-ion mode plasmas has been carried out to identify the most unstable micro-instabilities [25] using the initial value gyrokinetic code, GS2 [26], which finds the fastest growing mode. Local Miller equilibrium [27], with kinetic electrons and ions (including impurities and fast ions), full electromagnetic effects, and collisions were used in the simulations. Simulations were performed at three different locations, $\rho = 0.3$, 0.6 and 0.8, where ρ is the square root of the normalized magnetic flux, across both ion and electron scales from $10^{-2} \leqslant k_\theta \rho_{\mathrm{s}} \leqslant 10^2$ where k_θ is the poloidal wavenumber and ρ_{s} is the ion gyro-radius.

Figure 7 shows the linear growth rate, γ, and real frequency, ω, for a typical hot-ion mode pulse, #9831. The linear growth rates of both ion- and electron-scale (i.e. $k_\theta \rho_{\mathrm{s}} \geqslant 0.2$) modes decrease from the edge toward the core of the plasma, while at $\rho = 0.3$ the change of linear growth rates at $k_\theta \rho_{\mathrm{s}} < 0.2$ is non-monotonic (see figure 7(*a*)). Towards the plasma centre,

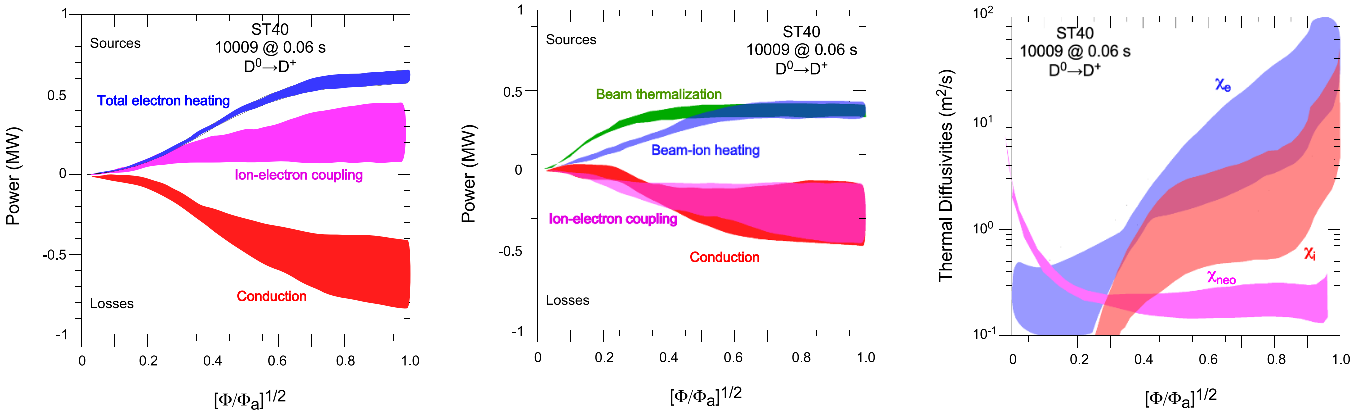

Figure 6. (left) Electron and (centre) ion power balances as functions of the square root of normalized toroidal flux. Positive values indicate energy sources, while negative values indicated energy losses. (right) Thermal diffusivity profiles as functions of the square root of normalized toroidal flux for electrons (blue) and ions (red). The ion neoclassical thermal diffusivity profile (pink) is also shown. Reproduced from [24].

$\rho = 0.3$, no unstable modes with $k_\theta \rho_s > 5$ were found and there was around an order of magnitude reduction in the maximum linear growth rate in the ion-scale range when compared to the outer region of the plasma. The maximum linear growth rates in the ion scale at all three locations are significantly higher than the corresponding Waltz-Miller E × B shearing rate, indicating that ion-scale modes may be important in driving transport in ST40 hot-ion mode plasmas.

The ω spectrum at $\rho = 0.3$ is seen in figure 7(*b*) to have a discontinuity between $k_\theta \rho_s = 0.2$ and 0.3, indicating the existence of two branches of solution of the dispersion relation. It is found through parametric scans that while the $k_\theta \rho_s \leqslant 0.2$ modes are likely to be kinetic ballooning modes (KBM), the $k_\theta \rho_s > 0.2$ modes are most likely to be the ion temperature gradient (ITG) mode or trapped electron mode (TEM). At mid and outer radii, $\rho = 0.6$ and 0.8, at electron scales the negative real frequency (propagating in the electron direction) and rapidly increasing ω with increasing $k_\theta \rho_s$ are consistent with drift wave characteristic of the electrostatic electron temperature gradient (ETG) mode. At intermediate length scales between ρ_i and ρ_e the ω spectrum displays very different characteristics, staying small over a wide range of wavenumbers ($k_\theta \rho_s$ from about 5–60 at $\rho = 0.8$ and from about 5–30 at $\rho = 0.6$), indicating the existence of a different, unidentified, instability in addition to the typically electrostatic ETG mode. At the ion scale, the dominant mode is identified as the ubiquitous mode (UM) [28], which is characterised by ω at $\rho = 0.8$ switching sign at $k_\theta \rho_s \approx 0.34$ from negative (electron direction) to positive (ion direction) as $k_\theta \rho_s$ increases from 0.05 to 2 (see the insert in figure 7(*b*)). Parametric scans in inverse aspect ratio and T_e and T_i gradients support the identification of UM at both $\rho = 0.8$ and 0.6, although at $\rho = 0.6$ the ω spectrum does not show a sign switching as at $\rho = 0.8$.

4.2. First measurements of confinement mass dependence

Kinetic profiles determined using the integrated data analysis workflow were the basis for studying the mass dependence of plasma confinement for the first time in any ST [24]. This was done using $H^0 \rightarrow H^+$, $D^0 \rightarrow H^+$, and $D^0 \rightarrow D^+$ plasmas. The central ion temperature was seen to increase from ∼5 keV to ∼10 keV with increasing plasma mass, and while the electron thermal conduction, as computed in TRANSP, was dominant, the increase in central ion temperature was driven by a reduction in core ion transport with increasing effective ion mass, M_{eff}, which overcompensated for the increased ion-electron collisional coupling as T_i, and thus $T_i - T_e$, increased with mass. This allowed the ions to decouple from the electrons. This reduced transport with increasing M_{eff} is reflected by the strong, near-linear dependence of thermal energy confinement time on M_{eff} (see figure 8). Additionally, higher T_i was observed at higher B_T for constant M_{eff}, and this dependence is coupled to a factor of several reduction in both core ion and electron thermal diffusivities at higher toroidal field in these $H^0 \rightarrow H^+$ plasmas. Although, the difference in T_i may also be attributed to differences in sawteeth activity in the discharges at these two toroidal fields.

5. Energetic particles

Experimentally, a distinction has been observed in terms of the Alfvénic nonlinear response in tokamaks of different aspect ratios. Spherical tokamaks tend to exhibit frequent Alfvénic chirping and avalanching, accompanied by wave amplitude bursting, while conventional tokamaks tend to have Alfvénic waves oscillating with a nearly fixed frequency and a quasi-steady amplitude [29]. This difference in behaviour has been attributed to microturbulence scattering of resonant fast ions. Anticipating the nonlinear character of Alfvénic instabilities is important in predicting the nature of fast ion losses, which can allow for the deployment of appropriate actuators to mitigate them. While chirping instabilities lead to convective transport, fixed-frequency ones lead to dominant diffusive losses as a result of mode overlapping.

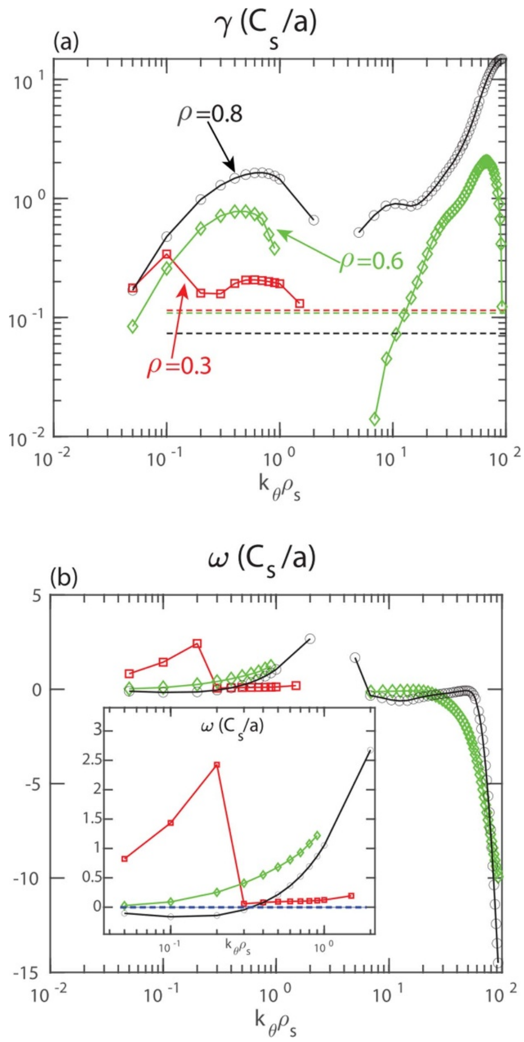

Figure 7. (*a*) Linear growth rate, γ, spectra and (*b*) real frequency, ω, spectra at $\rho = 0.3$ (red squares), 0.6 (green diamonds) and 0.8 (black circles). The horizontal dashed lines denote the Waltz-Miller $E \times B$ shearing rates at three radial locations with the same corresponding colours. The insert in (*b*) is a close-up view of the ion-scale ω, where the blue horizontal dashed line denotes $\omega = 0$. Modes with positive ω propagate in the ion diamagnetic direction and modes with negative ω propagate in the electron diamagnetic direction. Both γ and ω are expressed in the unit of the local C_s/a, where C_s is the ion sound speed with electron temperature and a is the half width of the last closed flux surface at the height of magnetic axis. Reproduced from [25].

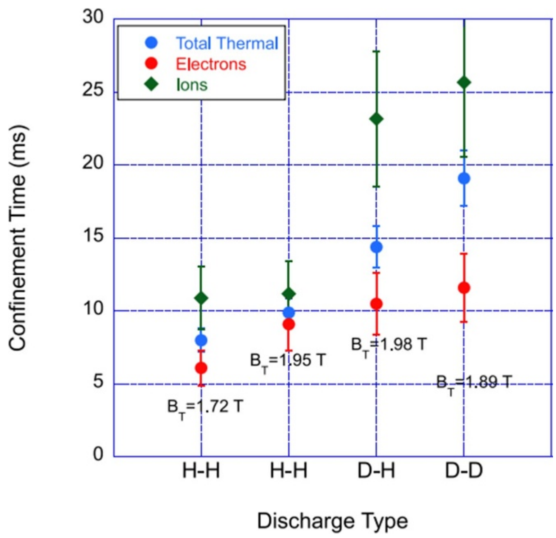

Figure 8. Electron, ion, and total thermal energy confinement as a function of plasma fuel species for high performance pulses. Reproduced from [24].

Two ST40 discharges, #9831 and #9894, that displayed a clear transition in their behaviour from the quasi-steady, fixed-frequency phase to the wave chirping phase are analysed in [30]. Kinetic and fast ion profiles from TRANSP were used as a basis for computing the linear Alfvénic continua by the ideal MHD code NOVA [31]. The most intense Alfvénic waves were identified as beta-induced Alfvén-acoustic eigenmode (BAAE) with toroidal mode number $n = 1$. BAAEs [32] are mixed Alfvén-acoustic polarization modes that reside in the gap that arises from the coupling between the acoustic and the Alfvénic continua. In both shots, a considerable reduction in ion transport, χ_i, as determined by TRANSP, precedes the emergence of chirping. In #9831 this reduction in χ_i is attributed to increased density peaking between 40 and 90 ms, which decreases the ion temperature gradient (ITG) drive associated with $\eta_i = |\nabla \ln T_i|/|\nabla \ln n_i|$. Relevant parameters from shot #9831 are shown in figure 9. In #9894, the density peaking remains approximately constant, however, there is a significant increase in toroidal beta, β_ϕ, which also acts to suppress ITG turbulence. A criterion for chirping likelihood implemented in NOVA-K, the kinetic post-processor of NOVA, correctly characterises the chirping response in these pulses.

In certain pulses, a possible interplay between these beam-driven BAAE modes and transitions between H and L-mode like confinement has been observed [33]. A small chirping (primer) mode of increasing amplitude was seen to build up during the H-mode confinement period, followed by a larger (dominant) chirping mode that initiates during the fast H-L transition and continues into the L-mode period. The chirping modes are also observed to systematically correlate with a decrease in toroidal plasma rotation, observed using the charge-exchange-recombination spectroscopy (CXRS) diagnostic. The NOVA code was used to determine the mode structure of the BAAE modes, which were found to have toroidal mode number $n = 1$ and a variety of poloidal mode numbers present, with the $m = 1$ harmonic having the strongest amplitude. The resonant beam-mode interaction was assessed with the initial value particle following code ASCOT [20] where simulations of the fast ion evolution were performed with an imposed $n = 1$, $m = 1$ perturbation of varying amplitudes. The fast particle content and corresponding torque were shown to decrease as the amplitude of the chirping perturbation is increased. The reduction in torque correlates with the experimentally observed reduction in plasma rotation, which could explain

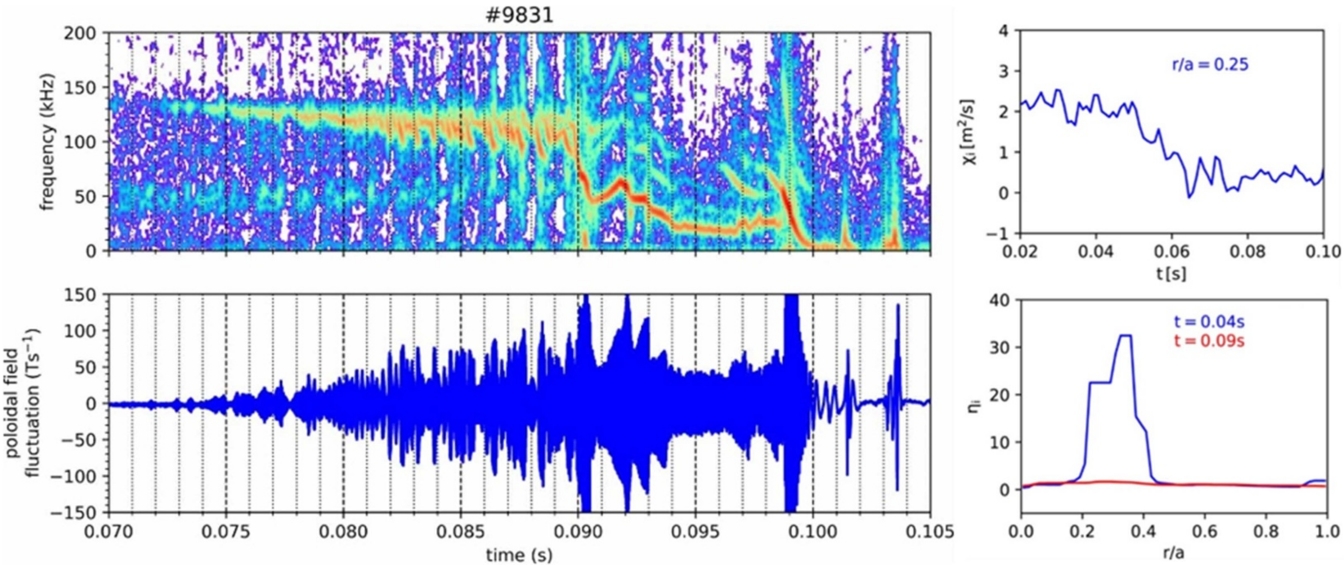

Figure 9. (Left-hand side) magnetic spectrogram and time-dependent poloidal field oscillation amplitude for discharge #9831. The transition from fixed frequency to chirping happens at around 0.08 s. (Top right) the inferred thermal ion heat conductivity at the radial location around the peak of the eigenstructure of the most unstable mode. (Bottom right) boxcar-smoothed $\eta_i = |\nabla \ln T_i|/|\nabla \ln n_i|$ before ($t = 0.04$ s) and after ($t = 0.09$ s) the transition to chirping. Reproduced from [30].

the degradation of edge transport barrier and transition back to L-mode.

6. Electron cyclotron assisted plasma start-up predictions

A multi-frequency electron cyclotron resonance heating (ECRH) and current drive (CD) system, employing a dual frequency 104/137 GHz gyrotron capable of delivering up to 1 MW of power, has been ordered and is due to be operational in 2025. The system is designed to enable the study of non-inductive plasma start-up, current ramp-up, and sustainment. It will consist of a poloidally and toroidally steerable low-field side (LFS) launcher that will allow conventional ECRH and CD schemes. A grooved mirror polarizer (MP) on the centre column provides the option of electron Bernstein wave (EBW) excitation via an O-X-B scheme, illustrated in figure 10. The mirror polarizer is made from molybdenum and is recessed below the centre column tiles and is therefore protected from direct exposure to the incoming plasma heat flux. O-mode is launched from the LFS onto the MP where it is converted to X-mode and propagates back into the plasma. The X-mode undergoes mode conversion to EBW at the upper hybrid resonance (UHR), which propagates towards the cyclotron resonance (ECR) where it is fully absorbed. Detailed modelling of the system has been conducted for various launch configurations [34, 35].

Conventional 2nd harmonic X-mode (X2) heating can be used for plasma heating and current sustainment. Modelling shows strong X2 absorption at a wide range of plasma densities and magnetic field strengths with modest current drive of

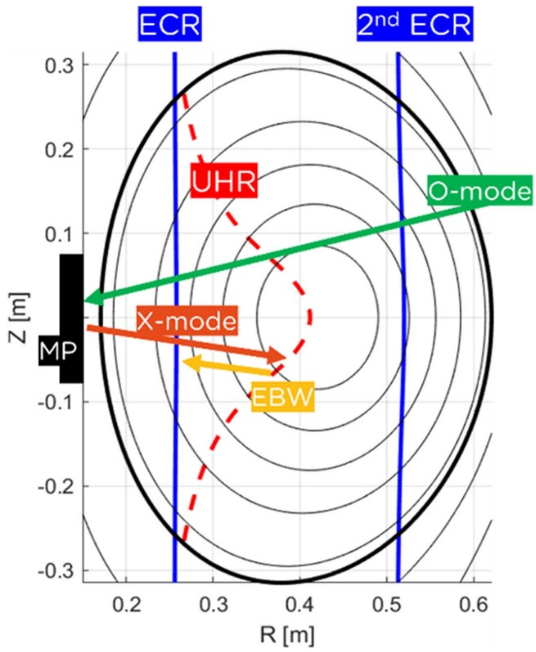

Figure 10. O-X-B scheme proposed on ST40 for the excitation of EBWs via a grooved mirror polarizer installed on the centre column.

up to 50 kA MW^{-1} expected [34]. Plasma start-up and ramp-up can be studied with the O-X-B scheme. EBWs are strongly absorbed, even at low densities and temperatures, and can generate strong current drive. Modelling has shown current drive efficiencies up to 150 kA MW^{-1} can be expected, depending on the density and temperature [34], as shown in figure 11. For the range of densities considered, $n_e = 0.5 - 3 \times 10^{19}\text{m}^{-3}$, the current drive efficiency peaks between $T_e = 2 - 3$ keV. At

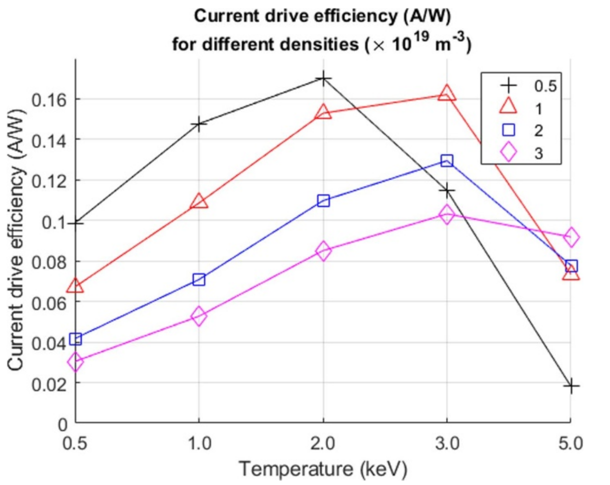

Figure 11. EBW current drive efficiency for different central electron densities (coloured lines and markers as indicated by the legend and in units of $10^{19}\ \mathrm{m}^{-3}$) as a function of central electron temperature. Reproduced from [34].

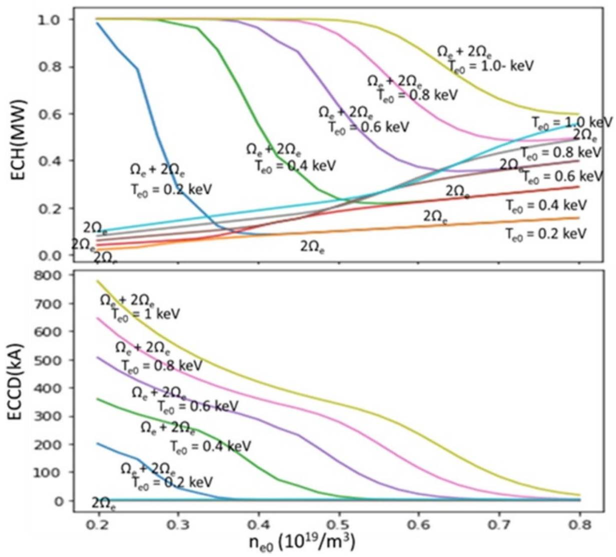

Figure 12. (Top) Absorbed power for 1MW of injected power for different central electron temperatures. The power shown is split into the sum of the fundamental (Ω_e) and 2nd harmonic ($2\Omega_e$) absorption, which represents the total absorbed power, and the power absorbed at the 2nd harmonic only. (Bottom) corresponding driven current, again separated into the sum of the fundamental and 2nd harmonic and 2nd harmonic only contributions. For the 2nd harmonic, the driven current is negligible. The toroidal magnetic field is $B_{\mathrm{T0}} = 2.3$ T and the radio-frequency wave has a frequency, $f = 105$ GHz and parallel refractive index $N_{\|0} = 0.3$. Reproduced from [35].

higher T_e, X-mode absorption at the ECR increases, reducing the power converted to EBW. As the current drive efficiency for X-mode is much less than EBW, the overall current drive decreases.

Additional, it was found that fundamental X-mode absorption could be used to generate significant current at low densities [35]. Typically X-mode injected from the LFS is reflected before it reaches the ECR, but it can be absorbed before the cut-off is reached if the Doppler shifted resonance condition $((\omega - \omega_{\mathrm{ce}})/(k_{\|} v_{\mathrm{th,e}}) \leqslant 3)$, is satisfied, where ω is the angular frequency of the injected wave, ω_{ce} is the electron cyclotron angular frequency, $k_{\|}$, is the parallel wave number, and $v_{\mathrm{th,e}}$ is the electron thermal velocity. Increasing the parallel wave number or temperature (and thus $v_{\mathrm{th,e}}$) will improve absorption. Figure 12 shows the absorption and current drive at different temperatures as a function of density. High current drive efficiencies up to 800 kA MW^{-1} can be achieved at low densities and high temperatures, with current drive decreasing with density and increasing with temperature. As density increases, absorption at the 2nd harmonic resonance, which is less efficient for current drive, increases, while fundamental absorption decreases.

7. Recent scenario development activities

The 2023 ST40 operational programme focused on exploring and expanding the range of achievable scenarios, with a particular focus on developing H-mode diverted scenarios and scenarios with high non-inductive current fractions. These scenarios will form the basis of future operational campaigns and enable ST40 to further advance the physics basis for the high field spherical tokamak.

7.1. H-mode diverted scenario development

During the most recent operational campaign diverted scenarios, in both double-null (DN) and upper single-null (USN) diverted configurations were developed. The DN plasmas were developed with elongations $\kappa \leqslant 2$, across a broad range of toroidal fields, $B_{\mathrm{T0}} = 0.9 - 2.1$ T, and plasma currents, $I_{\mathrm{p}} = 250 - 600$ kA. The USN scenarios have favourable ion ∇B drift (towards the x-point) and can be used to study the scrape-off layer heat flux width using the divertor diagnostics discussed in section 2.2. Several improvements to the plasma control system were made to expand the accessible operating space. This included restructuring the magnetic control scheme into inner and outer loops for fast vertical control, poloidal field coil current control, and main plasma parameter (total plasma current and plasma current centroid position [36]) control. Proportional-integral-derivative controllers were experimentally tuned and now feature bumpless transfer and anti-windup capabilities.

An example H-mode diverted plasma equilibrium and scenario for a beam heated scenario with $B_{\mathrm{T0}} = 1.8$ T and $I_{\mathrm{p}} = 400$ kA are shown in figures 13 and 14 respectively. The plasma becomes diverted at 70 ms and enters an ELM-free H-mode phase around 110 ms, shortly after the injection of the 24 kV neutral beam, which persists until the beam power is reduced. Preliminary electron temperature and density profiles measured with the recently installed Thomson scattering

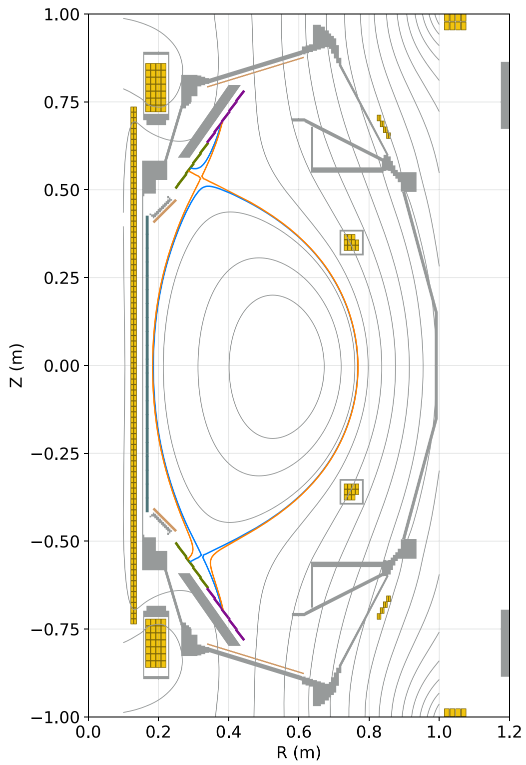

Figure 13. Example H-mode plasma equilibrium, from pulse #11418. EFIT equilibrium at 150 ms showing plasma in a DN configuration with a slight bias towards the lower divertor. The blue and orange contours shows the last-closed-flux-surface (LCFS) for the primary (active) and secondary (in-active) x-points respectively.

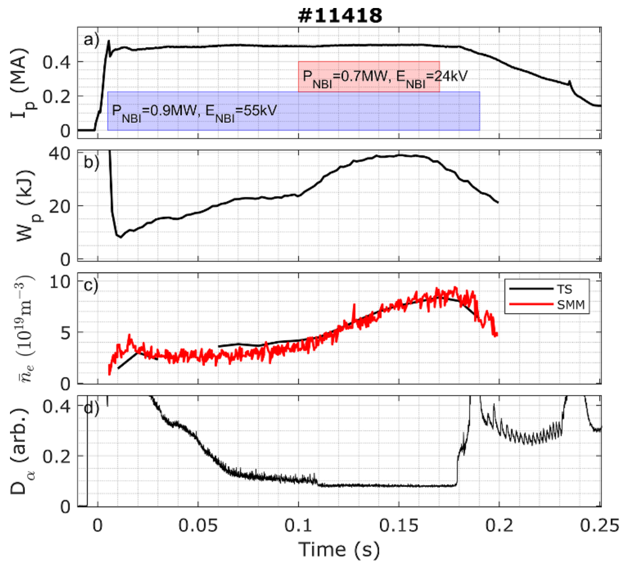

Figure 14. Example H-mode scenario, from pulse #11418. (*a*) plasma current from EFIT and neutral beam parameters, (*b*) stored energy from EFIT, W_p, (*c*) line integrated electron density, $\bar{n}_e$, from preliminary TS data (black) and radial sub millimetre (SMM) interferometer (red) (*d*) D_α signal. The transition to H-mode occurs at around 110 ms and can be seen by the reduction in D_α, increase in W_p and $\bar{n}_e$, and formation of a pedestal, shown in figure 15.

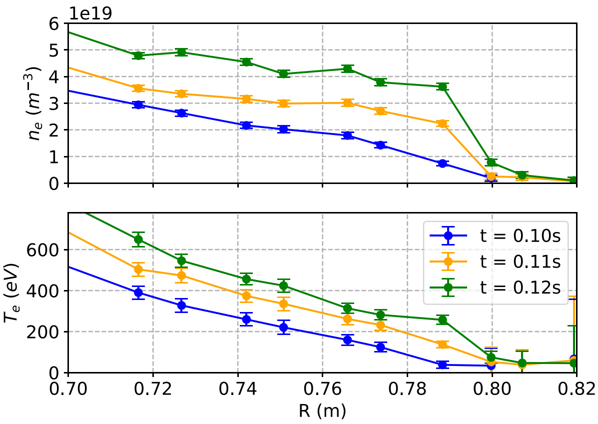

Figure 15. Thomson scattering density and temperature profiles for pulse #11418 around the time of the L-H transition, which occurs at around 110 ms. The formation of the pedestal can be seen with the final pedestal top parameters being $n_{e,ped} \approx 4 \times 10^{19}$m^{-3} and $T_{e,ped} \approx 200$ eV.

system are shown in figure 15 around the time of the L-H transition. For the H-mode scenarios developed, typical pedestal top densities and temperatures are in the range of $n_{e,ped} \approx 3.5 - 5.5 \times 10^{19}$ m^{-3} and $T_{e,ped} \approx 200$ eV. These ELM free periods appear to be a feature of ST40 plasmas and are present in the majority of H-mode scenarios developed thus far. ELM-free H-modes have been observed on other devices, such as C-Mod [37, 38], ASDEX-U [39], DIII-D [40] and NSTX [41]. Further work is required to characterise these operating modes and determine their classification.

Across the range of toroidal magnetic fields and densities achievable, the fast ions from both the 55 kV and 24 kV beams can be born with either super- or sub-Alfvénic velocities, $v_A = B/\sqrt{\mu_0 m_i n_i}$. This, combined with the high beam power densities, means ST40 is well placed to explore fast ion instabilities and the resulting fast ion transport and losses in spherical tokamaks. In upcoming operations, these scenarios will be used to study confinement and stability, and plasma exhaust properties across a broad range of plasma parameters, building on the work discussed above.

7.2. Non-inductive scenario development

Simulations have shown that non-inductive current fractions of more than 70% should be attainable in ST40 with both beams at a plasma current of around 250 kA. The bootstrap fraction, f_{bs}, is proportional to beta poloidal, β_p, which is confinement rather than stability limited in the target range ($f_{bs} > 50\%$, $\beta_p \sim 1.5$ and $B_{T0} = 1.8$ T). Both limiter and diverted H-mode plasmas have been obtained with $I_p \approx 300$ kA, in which the Ohmic solenoid swing is halted or even reversed during the pulse. Thus far, the highest performance has been achieved in the limiter configuration discharges. During the period of low or reversed surface loop voltage the plasma stored energy reaches $W_{th} \approx 35$ kJ, with corresponding poloidal and normalised betas of $\beta_p \sim 1.4$ and $\beta_N \sim 4.4$ respectively. These plasmas are highly dynamic, having rapidly increasing energy content and density, although the plasma current is constant. Stability analysis has shown that the limiter discharges plasma exceed the no-wall beta stability limit, which then terminated the H-mode. The diverted plasmas entered the H-mode late in the neutral beam pulse and were still evolving when the neutral beam pulse ended. The planned extension to the duration of the 24 kV neutral beam should enable these pulses to reach more static conditions and for the period of low loop voltage to be extended.

8. Conclusions and outlook

ST40 is expanding the physics and technology basis for the spherical tokamak route to commercial fusion energy, and during the last two years of plasma operations has made substantial progress in this area.

Record plasma ion temperatures of 9.6 ± 0.4 keV have been achieved in hot-ion mode regimes, demonstrating for the first time that commercial fusion relevant ion temperatures can be obtained in a compact high-field spherical tokamak. Ion temperatures in the 10 keV range have only previously been obtained in significantly larger devices and never in a ST. These high temperature plasmas had a corresponding fusion triple product of $n_{i0}T_{i0}\tau_E \approx 6 \pm 2 \times 10^{18}$ m^{-3}keVs. Transport analysis showed that the core ion thermal diffusivity was very low, reflecting the fact that reduced central ion transport was largely responsible for the high central ion temperatures. Linear gyrokinetic analysis revealed that a range of micro-instabilities were present, including kinetic ballooning, ion temperature gradient and trapped electron modes in the core and electron temperature gradient and ubiquitous modes at mid to outer radius.

By developing scenarios with different main plasma and beam species the mass dependence of thermal energy confinement was investigated for the first time in any ST and found to have a strong near-linear dependence on the effective ion mass.

Energetic particle studies investigated pulses that displayed a clear transition in their nonlinear Alfvénic response from a quasi-steady, fixed frequency phase to a wave chirping phase. The difference in response has previous been attributed to microturbulence scattering of resonant fast ions. This behaviour was confirmed on ST40, with the transition from fixed frequency to chirping corresponding to a reduction in microturbulence, and a criterion for determining the likelihood of chirping correctly characterised the response.

Recent ST40 operations have focused on expanding the operating space by developing diverted H-mode plasmas across a range of magnetic fields and plasmas currents, as well as establishing scenarios with a high non-inductive current fraction. Both DN and USN diverted configurations have been established, with the DN diverted scenarios developed over a broad range of toroidal magnetic fields, $B_{T0} = 0.9 - 2.1$ T, and plasma currents, $I_p = 250 - 600$ kA. These diverted H-mode plasmas typically feature sustained ELM free periods, and further work is required to characterise these operating modes. For the non-inductive scenarios, thus far the highest performance has been achieved in discharges with a limiter configuration. These plasmas had $I_p \approx 300$ kA and had periods where the Ohmic solenoid swing was halted or even reversed. During this period, the plasma is highly dynamic and the normalised beta reached $\beta_N \sim 4.4$, which stability analysis has shown exceeds the no-wall beta stability limit, and led to the termination of the pulse. In the next operational phase, planned for 2024, these scenarios will be used to explore confinement and stability at magnetic fields higher than that achieved in other spherical tokamaks and to investigate exhaust properties in a compact, high power density device.

Following the 2024 operational period, a 1 MW dual frequency (104/137 GHz) gyrotron will be installed to enable the study of non-inductive plasma start-up, current ramp-up and sustainment, and to extend confinement, stability and exhaust studies to plasmas with dominant electron heating. Three electron cyclotron (EC) current drive schemes have been investigated, conventional 2nd harmonic X-mode low field side launch; an O-X-B scheme for exciting electron Bernstein waves that uses a mirror polariser mounted on the centre post; and a fundamental X-mode scheme that utilises the strong Doppler shift of the resonance location that occurs at low densities and high electron temperatures. These schemes are predicted to have peak current drive efficiencies of 50, 150 and 800 kA MW^{-1} respectively.

Acknowledgments

Contributions from collaborators at Princeton Plasma Physics Laboratory and Oak Ridge National Laboratory were supported through U.S. Department of Energy CRADA NFE-19-07769. The 24 kV neutral beam system was provided on loan from Consorzio RFX.

ORCID iDs

S.A.M. McNamara https://orcid.org/0000-0002-0477-5247
A. Alieva https://orcid.org/0000-0002-4573-4951
M.S. Anastopoulos Tzanis https://orcid.org/0000-0001-6564-3152
O. Asunta https://orcid.org/0000-0001-5618-5380
J. Bland https://orcid.org/0000-0002-4083-7812
H. Bohlin https://orcid.org/0000-0001-6637-5460
P.F. Buxton https://orcid.org/0000-0002-0349-0434
C. Colgan https://orcid.org/0000-0001-6227-2317
A. Dnestrovskii https://orcid.org/0000-0002-4827-9421
E. du Toit https://orcid.org/0000-0003-4383-8906
M. Fontana https://orcid.org/0000-0002-7979-7483
M. Gemmell https://orcid.org/0009-0003-2469-3665
M.P. Gryaznevich https://orcid.org/0000-0002-4518-5593
J. Hakosalo https://orcid.org/0009-0009-6547-3128
M.R. Hardman https://orcid.org/0000-0001-5152-3061

D. Harryman https://orcid.org/0000-0002-1194-9081
D. Hoffman https://orcid.org/0000-0001-6898-7807
M. Iliasova https://orcid.org/0000-0003-3170-1507
S. Janhunen https://orcid.org/0000-0002-8022-0825
F. Janky https://orcid.org/0009-0001-9488-7188
H.F. Lowe https://orcid.org/0000-0002-9085-1073
E. Maartensson https://orcid.org/0009-0000-7289-8516
C. Marsden https://orcid.org/0000-0003-1322-5236
S.Y. Medvedev https://orcid.org/0000-0002-9358-9402
S.R. Mirfayzi https://orcid.org/0000-0003-4628-796X
M. Moscheni https://orcid.org/0000-0002-6355-7274
G. Naylor https://orcid.org/0009-0009-0279-4506
V. Nemytov https://orcid.org/0009-0007-6490-2635
T. O'Gorman https://orcid.org/0009-0006-8803-015X
D. Osin https://orcid.org/0009-0005-7678-4467
T. Pyragius https://orcid.org/0000-0002-4388-2600
A. Rengle https://orcid.org/0009-0001-9037-1125
M. Romanelli https://orcid.org/0000-0003-4897-4843
C. Romero https://orcid.org/0009-0004-2032-5213
M. Sertoli https://orcid.org/0000-0003-1528-6307
V. Shevchenko https://orcid.org/0009-0007-4795-8717
J. Sinha https://orcid.org/0000-0002-9721-769X
A. Sladkomedova https://orcid.org/0000-0002-0012-9328
S. Sridhar https://orcid.org/0000-0002-7458-8092
J. Stirling https://orcid.org/0009-0002-9123-6379
Y. Takase https://orcid.org/0000-0002-4846-5267
P.R. Thomas https://orcid.org/0000-0002-9663-685X
J. Varje https://orcid.org/0000-0003-4137-2436
E. Vekshina https://orcid.org/0000-0001-9771-5579
B. Vincent https://orcid.org/0009-0009-5293-444X
H.V. Willett https://orcid.org/0000-0002-4324-3438
J. Wood https://orcid.org/0009-0006-0391-2250
E. Wooldridge https://orcid.org/0009-0006-7042-2569
D. Zakhar https://orcid.org/0009-0006-6442-1367
X. Zhang https://orcid.org/0000-0003-3775-5821
D. Battaglia https://orcid.org/0000-0001-8897-9740
N. Bertelli https://orcid.org/0000-0002-9326-7585
P.J. Bonofiglo https://orcid.org/0000-0001-5057-7383
L.F. Delgado-Aparicio https://orcid.org/0000-0001-6739-4380
V.N. Duarte https://orcid.org/0000-0001-8096-7518
N.N. Gorelenkov https://orcid.org/0000-0002-7345-8149
M. de Haas https://orcid.org/0009-0002-3931-7761
S.M. Kaye https://orcid.org/0000-0002-2514-1163
R. Maingi https://orcid.org/0000-0003-1238-8121
D. Mueller https://orcid.org/0000-0002-2456-3356
M. Ono https://orcid.org/0000-0001-9849-9417
M. Podesta https://orcid.org/0000-0003-4975-0585
Y. Ren https://orcid.org/0000-0003-4571-9046
S. Trieu https://orcid.org/0000-0002-1279-670X
E. Delabie https://orcid.org/0000-0001-9834-874X
T.K. Gray https://orcid.org/0000-0001-8220-8195
B. Lomanowski https://orcid.org/0000-0003-2226-2004
E.A. Unterberg https://orcid.org/0000-0003-1353-8865
O. Marchuk https://orcid.org/0000-0001-6272-2605

References

[1] Peng Y.K.M. and Strickler D.J. 1986 Features of spherical torus plasmas *Nucl. Fusion* **26** 769
[2] Kaye S.M., Connor J.W. and Roach C.M. 2021 Thermal confinement and transport in spherical tokamaks: a review *Plasma Phys. Control. Fusion* **63** 123001
[3] Salmi A., Gryaznevich M.P., Buxton P.F., Nightingale M. and Tala T. 2017 Neutral beam optimisation for the spherical tokamak ST40 *Fusion Eng. Des.* **117** 14–19
[4] Sykes A. *et al* 1992 First results from the START experiment *Nucl. Fusion* **32** 694
[5] Sykes A. *et al* 2001 First results from MAST *Nucl. Fusion* **41** 1423
[6] Ono Y., Hayashi Y., Ii T., Tanabe H., Ito S., Kuwahata A., Ito T., Kamino Y., Yamada T. and Inomoto M. 2011 Intermittent magnetic reconnection in TS-3 merging experiment *Phys. Plasmas* **18** 111213
[7] Chung K.J., An Y.H., Jung B.K., Lee H.Y., Sung C., Na Y.S., Hahm T.S. and Hwang Y.S. 2013 Design features and commissioning of the versatile experiment spherical torus (VEST) at seoul national university *Plasma Sci. Technol.* **15** 244
[8] Gryaznevich M.P. and Sykes A. 2017 Merging-compression formation of high temperature tokamak plasma *Nucl. Fusion* **57** 072003
[9] Nagy A., Bortolon A., Mauzey D.M., Wolfe E., Gilson E.P., Lunsford R., Maingi R., Mansfield D.K., Nazikian R. and Roquemore A.L. 2018 A multi-species powder dropper for magnetic fusion applications *Rev. Sci. Instrum.* **89** 10K121
[10] Lao L.L., St John H., Stambaugh R.D., Kellman A.G. and Pfeiffer W. 1985 Reconstruction of current profile parameters and plasma shapes in tokamaks *Nucl. Fusion* **25** 1611
[11] Harryman D.M., Colgan C., Lovell J., Moscheni M., Naylor G., Rengle A., Sertoli M., Sladkomedova A. and Thwaites R. 2024 Design and commissioning of resistive foil bolometer diagnostics on the ST40 tokamak *Rev. Sci. Instrum.* **95** 083534
[12] Iliasova M.V. *et al* 2024 Characterisation of diamond and organic scintillation detectors utilising radiation sources for continuous plasma operation *Rev. Sci. Instrum.* Submitted
[13] Wood J., Lomanowski B., Delabie E., Willett H.V., Sertoli M. and Varje J. 2023 Characterisation of ion temperature and toroidal rotation on the ST40 tokamak *J. Instrum.* **18** C03019
[14] Willett H.V., Osin D., Naylor G., Wood J., Lomanowski B. and Sertoli M. 2023 TriWaSp: a multi-faceted visible spectroscopy diagnostic on the ST40 tokamak *J. Instrum.* **18** C03023
[15] Lowe H.F. *et al* 2023 First measurements of electron temperature and density profiles using Thomson scattering on the ST40 spherical tokamak *20th Int. Symp. on Laser-Aided Plasma Diagnostics* (*Kyoto, Japan, 10–14 September 2023*) (available at: https://lapd20.nifs.ac.jp/) (Accessed August 2024)
[16] Eich T. *et al* 2013 Scaling of the tokamak near the scrape-off layer H-mode power width and implications for ITER *Nucl. Fusion* **53** 093031
[17] Sertoli M. *et al* 2024 From MVPs to full models: a step-wise development of diagnostic forward models in support of design, analysis and modelling on the ST40 tokamak *Plasma Phys. Control. Fusion* **66** 095011
[18] Open-ADAS 2022 (available at: https://open.adas.ac.uk) (Accessed October 2022)

[19] Geiger B. *et al* 2020 Progress in modelling fast-ion D-alpha spectra and neutral particle analyzer fluxes using FIDASIM *Plasma Phys. Control. Fusion* **62** 105008
[20] Varje J., Särkimäki K., Kontula J., Ollus P., Kurki-Suonio T., Snicker A., Hirvijoki E. and Äkäslompolo S. 2019 High-performance orbit-following code ASCOT5 for Monte Carlo simulations in fusion plasmas (arXiv:1908.02482)
[21] Pankin A., McCune D., Andre R., Bateman G. and Kritz A. 2004 The tokamak Monte Carlo fast ion module NUBEAM in the national transport code collaboration library *Comput. Phys. Commun.* **159** 157–84
[22] McNamara S.A.M. *et al* 2023 Achievement of ion temperatures in excess of 100 million degrees Kelvin in the compact high-field spherical tokamak ST40 *Nucl. Fusion* **63** 054002
[23] Hawryluk R.J. 1981 An empirical approach to tokamak transport *Physics of Plasmas Close to Thermonuclear Conditions* (Elsevier) pp 19–46 (available at: https://transp.pppl.gov/) (Accessed August 2024)
[24] Kaye S.M., Sertoli M., Buxton P.F., Dnestrovskii A., McNamara S.A.M., Romanelli M. and Thomas P. 2023 Isotope dependence of transport in ST40 hot ion mode plasmas *Plasma Phys. Control. Fusion* **65** 095012
[25] Ren Y., Kaye S.M., Anastopoulos Tzanis M.S., Sertoli M., Dnestrovskii A. and Romanelli M. (the ST40 Team) 2023 Linear instabilities in the hot-ion regime in a high-field spherical tokamak *Plasma Phys. Control. Fusion* **65** 075007
[26] Kotschenreuther M., Rewoldt G. and Tang W.M. 1995 Comparison of initial value and eigenvalue codes for kinetic toroidal plasma instabilities *Comput. Phys. Commun.* **88** 128–40
[27] Miller R.L., Chu M.S., Greene J.M., Lin-Liu Y.R. and Waltz R.E. 1998 Noncircular, finite aspect ratio, local equilibrium model *Phys. Plasmas* **5** 973–8
[28] Coppi B. and Pegoraro F. 1977 Theory of the ubiquitous mode *Nucl. Fusion* **17** 969
[29] Duarte V.N., Berk H.L., Gorelenkov N.N., Heidbrink W.W., Kramer G.J., Nazikian R., Pace D.C., Podesta M., Tobias B.J. and Van Zeeland M.A. 2017 Prediction of nonlinear evolution character of energetic-particle-driven instabilities *Nucl. Fusion* **57** 054001
[30] Duarte V.N., Gorelenkov N.N., Kaye S.M., Bonofiglo P.J., Podestà M., Bland J., Buxton P., Gryaznevich M.P., Romanelli M. and Sertoli M. 2023 Perturbative analysis of low-frequency instabilities in high-field ST40 experiments *Nucl. Fusion* **63** 036018
[31] Cheng C.Z., Chen L. and Chance M.S. 1985 High-n ideal and resistive shear Alfvén waves in tokamaks *Ann. Phys., NY* **161** 21–47
[32] Gorelenkov N.N., Berk H.L., Fredrickson E. and Sharapov S.E. and (JET EFDA Contributor) 2007 Predictions and observations of low-shear beta-induced shear Alfvén–acoustic eigenmodes in toroidal plasmas *Phys. Lett.* A **370** 70–77
[33] Bland J, Varje J., Gorelenkov N.N., Gryaznevich M.P., Sharapov S.E. and Wood J. (the ST40 Team) 2022 Interplay between beam-driven chirping modes and plasma confinement transitions in spherical tokamak ST40 *Nucl. Fusion* **63** 016024
[34] du Toit E.J. and Shevchenko V.F. 2022 Development of an electron cyclotron resonance heating and electron Bernstein wave current drive system on ST40 *Plasma Phys. Control. Fusion* **64** 115015
[35] Ono M., Bertelli N. and Shevchenko V.F. 2022 Multi-harmonic electron cyclotron heating and current drive scenarios for non-inductive start-up and ramp-up in high field ST40 spherical tokamak *Nucl. Fusion* **62** 106035
[36] De Tommasi G. 2019 Plasma magnetic control in tokamak devices *J. Fusion Energy* **38** 406–36
[37] Greenwald M. *et al* 1999 Characterization of enhanced D_α high-confinement modes in Alcator C-Mod *Phys. Plasmas* **6** 1943–9
[38] Takase Y. *et al* 1997 Radiofrequency-heated enhanced confinement modes in the Alcator C-Mod tokamak *Phys. Plasmas* **4** 1647–53
[39] Gil L. *et al* 2020 Stationary ELM-free H-mode in ASDEX Upgrade *Nucl. Fusion* **60** 054003
[40] Osborne T.H. *et al* 2015 Enhanced H-mode pedestals with lithium injection in DIII-D *Nucl. Fusion* **55** 063018
[41] Maingi R. *et al* 2009 Edge-localized-mode suppression through density-profile modification with lithium-wall coatings in the National Spherical Torus Experiment *Phys. Rev. Lett.* **103** 075001